JULY 2021

Obstinct Controls on the Strength of the Abyssal Overturning Circulation: Channel versus Basin Dynamics

CHIUNG-YIN CHANG^a AND MALTE F. JANSEN^a

^a Department of the Geophysical Sciences, University of Chicago, Chicago, Illinois

(Manuscript received 23 December 2020, in final form 8 March 2021)

ABSTRACT: Although the reconfiguration of the abyssal overturning circulation has been argued to be a salient feature of Earth's past climate changes, our understanding of the physical mechanisms controlling its strength remains limited. In particular, existing scaling theories disagree on the relative importance of the dynamics in the Southern Ocean versus the dynamics in the basins to the north. In this study, we systematically investigate these theories and compare them with a set of numerical simulations generated from an ocean general circulation model with idealized geometry, designed to capture only the basic ingredients considered by the theories. It is shown that the disagreement between existing theories can be partially explained by the fact that the overturning strengths measured in the channel and in the basin scale distinctly with the external parameters, including surface buoyancy loss, diapycnal diffusivity, wind stress, and eddy diffusivity. The overturning in the reentrant channel, which represents the Southern Ocean, is found to be sensitive to all these parameters, in addition to a strong dependence on bottom topography. By contrast, the basin overturning varies with the integrated surface buoyancy loss rate and diapycnal diffusivity but is mostly unaffected by winds and channel topography. The simulated parameter dependence of the basin overturning can be described by a scaling theory that is based only on basin dynamics.

KEYWORDS: Abyssal circulation; Meridional overturning circulation; Ocean dynamics

1. Introduction

The abyssal ocean is a large reservoir of heat and carbon for the climate system, and the abyssal overturning circulation has often been hypothesized to be a key player that has modulated climate feedbacks during past climate changes (e.g., Adkins 2013, and references therein). Despite its importance, the mechanisms that govern these changes in the abyssal overturning circulation remain poorly understood.

The classic theoretical picture for the abyssal overturning circulation, still found in textbooks, is built on the early work by Stommel and Munk. Stommel (1961) proposed a two-box model to illustrate the role of temperature and salinity forcing on the overturning circulation, although ocean dynamics and mixing processes that are crucial to return the deep water to the surface are treated implicitly. Munk (1966) and Munk and Wunsch (1998) focused on the buoyancy budget of the abyssal upwelling, assuming it to be uniform throughout the basin and constrained by the balance between vertical advection and turbulent diapycnal diffusion. Stommel and Arons (1959) investigated the horizontal structure of the abyssal circulation, based on the vorticity dynamics in a closed basin, but the rate of deep water formation must be prescribed in their theory.

The modern literature on the abyssal overturning circulation has come to a general agreement that the minimum conceptual model to represent its dynamics should account for not only a basin but also a circumpolar channel representing the Southern

denotes content that is immediately available upon publication as open access.

Corresponding author: Chiung-Yin Chang, cyinchang@uchicago.edu

Stewart et al. 2014). This view accounts for the fact that a large amount of deep water upwells to the surface in the Southern Ocean. The Southern Ocean circulation is driven by Ekman pumping and suction, which highlights the potential role of wind stress forcing, in addition to the buoyancy forcing and turbulent mixing considered in the classical models (Lumpkin and Speer 2007; Marshall and Speer 2012; Talley 2013, and references therein).

Building upon these findings, recent theories for the dy-

Ocean (e.g., Toggweiler and Samuels 1995; Ito and Marshall 2008; Nikurashin and Vallis 2011; Shakespeare and Hogg 2012;

Building upon these findings, recent theories for the dynamics of the abyssal overturning circulation have put the most emphasis on the roles of wind stress and baroclinic eddies in the Southern Ocean (Ito and Marshall 2008; Nikurashin and Vallis 2011; Mashayek et al. 2015). In these theories, it is implicitly assumed that the dynamics in the basin are not essential to constraining the circulation, although the thermodynamics in the basin are relevant. Specifically, Nikurashin and Vallis (2011) developed a scaling theory that matches the wind- and eddy-driven circulation derived from the momentum budget in the Southern Ocean, to a basin that is effectively a onedimensional advective-diffusive model as envisioned in Munk (1966). Mashayek et al. (2015) suggested improvements by pointing out the necessity of horizontal advection in maintaining the buoyancy budget in the abyssal boundary layer, but the resulting scaling relations do not change fundamentally, as will be discussed below. In both studies, the proposed scaling relations are compared with three-dimensional numerical simulations with an idealized model geometry that consists of a basin and a channel. The simulations confirm the theoretical predictions, indicating that the basin dynamics may indeed be unimportant.

On the other hand, there are scaling theories that focus on the dynamics in the basin, while not explicitly considering the momentum budget in the Southern Ocean (Kamenkovich and

DOI: 10.1175/JPO-D-20-0316.1

Goodman 2000; Jansen and Nadeau 2016, hereinafter JN16). The argument of JN16 is motivated by a need to better understand the circulation impact of a changing surface buoyancy loss around Antarctica (e.g., Shin et al. 2003; Shakespeare and Hogg 2012; Stewart et al. 2014; Ferrari et al. 2014; Watson et al. 2015; Sun et al. 2016). None of the previously discussed channelbased scaling theories (Ito and Marshall 2008; Nikurashin and Vallis 2011; Mashayek et al. 2015) predict the effect on the circulation of changes in the surface buoyancy loss, and JN16 argued that to do so one cannot avoid discussing basin dynamics. While not a closed theory, they accordingly derived a scaling relation that is substantially different from the theories considering the channel dynamics and points toward the important role of the net surface buoyancy loss in the region of bottom water formation. They also confirmed that their scaling is generally supported by their numerical simulations. However, an apparent discrepancy exists between JN16's theory, which focuses on basin dynamics, and the other existing theories, which focus on channel dynamics.

This study aims to explain this discrepancy by testing the theories and their assumptions with the help of numerical simulations of an idealized model. To ensure that these simulations consist of the essential physics only, we employ a model configuration that is purposely chosen to eliminate complexities that are not taken into account in any of the theories. Taking advantage of this simplicity, we then examine the changes in the abyssal circulation with various parameters and compare the results with the scaling theories. We primarily focus on assessing the theoretical predictions for the overturning strength of the abyssal circulation, as its changes appear to be more robustly defined than other potentially interesting aspects of circulation changes.

The rest of the paper is organized in the following way. The existing theories are formally introduced in section 2, and an extension to close the scaling of JN16 is proposed. Section 3 describes the setup of our model simulations, the parameter range explored, and the details of the diagnostics performed. Section 4 then compares the existing theories with the simulations. In section 5, we investigate the extent to which the results are modified in the presence of bottom topography in the channel. Section 6 summarizes our findings and concludes with some questions for future work.

2. Existing theories for overturning strength

a. Decomposition of the residual streamfunction

The strength of the abyssal overturning circulation will be measured by the residual streamfunction, $\Psi(y,z)$, which is in turn defined as the isopycnal streamfunction, $\Psi^{\dagger}(y,b)$, remapped from buoyancy (b) coordinates to depth (z) coordinates. The theories we examine in this study are derived from (and compared with) idealized models that do not resolve mesoscale eddies. The Gent–McWilliams (GM) scheme is adopted in these models to parameterize the meridional transport by mesoscale eddies, $v^{\rm GM} \equiv -\partial_z(K\partial_y z|_b)$ with K being the GM diffusivity (Gent and McWilliams 1990). Since resolved transient eddies are generally negligible in coarse-resolution simulations that employ the GM parameterization, the total meridional transport can be approximated as $v^{\rm total} \approx \overline{v} + \overline{v}^{\rm GM}$,

with the overbar denoting a time average. We therefore compute the isopycnal streamfunction as

$$\Psi^{\dagger}(y,b) = -\int_{b_{\min}}^{b} \oint (\overline{v} + \overline{v}^{GM}) \frac{\partial \overline{z}}{\partial b} dx \, db. \tag{1}$$

To obtain the residual streamfunction in depth-latitude space, we remap the isopycnal streamfunction at a given $b = \hat{b}$ to its mean isopycnal depth $z = [z(\hat{b})]$, with the bracket denoting the zonal mean (e.g., Young 2012). Accordingly, we can then obtain the residual streamfunction as

$$\Psi(y,z) \equiv \Psi^{\dagger}(y,\hat{b}(z)). \tag{2}$$

An example of the isopycnal and corresponding residual streamfunction is shown in Fig. 1, which we will describe later on in further detail.

To derive a theory for the residual streamfunction, it is useful to decompose it into several components that represent different physical processes. The specific decomposition adopted here is

$$\Psi(y, z) = \Psi^{EU}(y, z) + \Psi^{GM}(y, z) + \Psi^{ST}(y, z), \tag{3}$$

where Ψ^{EU} is the Eulerian mean streamfunction, Ψ^{GM} is the GM streamfunction that represents the parameterized transport by transient mesoscale eddies, and Ψ^{ST} is the stationary eddy streamfunction due to any zonal asymmetry of the flow. Unlike the residual streamfunction, the Eulerian mean streamfunction, and the GM streamfunction, are defined by zonally integrating the meridional transport at fixed depth:

$$\Psi^{\text{EU}}(y,z) = \int_{-H}^{z} \oint \overline{v} \, dx \, dz \quad \text{and}$$
 (4)

$$\Psi^{\rm GM}(y,z) = \int_{-H}^{z} \oint \overline{v}_{\rm GM} \, dx \, dz. \tag{5}$$

The standing eddy contribution is then defined as the difference between the zonally integrated transport at fixed buoyancy and transport integrated at fixed depth: $\Psi^{\rm ST}(y,z)=\Psi(y,z)-(\Psi^{\rm EU}(y,z)+\Psi^{\rm GM}(y,z))$. A summary of the different streamfunction notations and their definitions is provided in Table 1 for easy reference. These different streamfunction notations will be repeatedly brought up in the discussion, since Eq. (3) is the starting point of the existing theories for the abyssal overturning strength, as will be explained in the following.

b. Scaling relations based on channel dynamics

We first consider the existing scaling theories that are based on the dynamics in the channel and summarized in Table 2: Ito and Marshall (2008), Nikurashin and Vallis (2011), and Mashayek et al. (2015) (hereinafter collectively referred to as INM). Although the specific derivations in INM differ somewhat, the resulting scaling relations are similar, and will be rederived here. One challenge for the derivation of a scaling theory based on Eq. (3) is that, although the residual circulation is approximately constant along isopycnals below the surface layer in the channel if diabatic transformations are small, the individual terms on the rhs of Eq. (3) generally vary substantially. Averaging Eq. (3) meridionally along isopycnals in the channel alleviates this issue, while allowing us to relate the

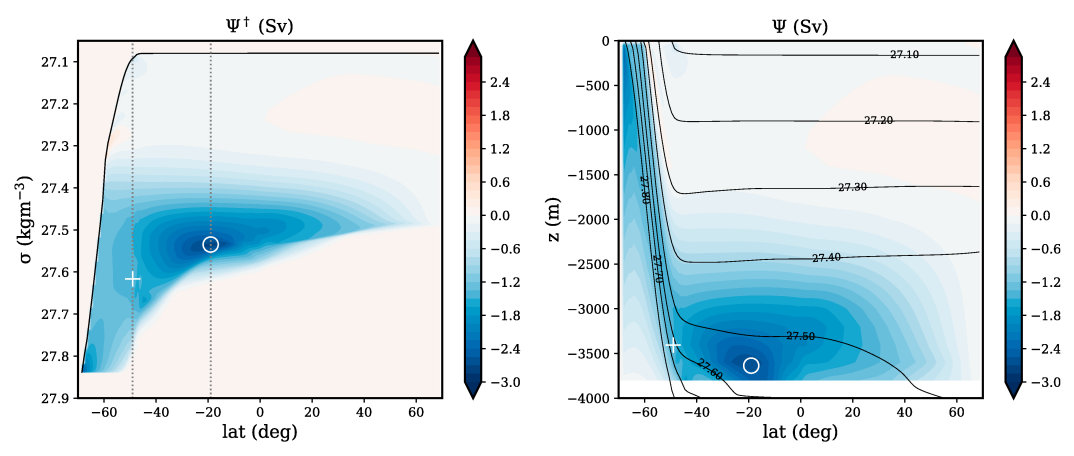


Fig. 1. Overturning circulation in the control simulation: (left) $\Psi^{\dagger}(y,b)$ with the black line indicating the maximum surface density for a given latitude; (right) $\Psi(y,z)$ with black lines indicating the zonally averaged depth of a given isopycnal. For illustration purposes, buoyancy values have here been translated into potential densities σ , using $\delta\sigma = -g^{-1}\rho_0\delta b$, with g = 9.81 m s⁻², $\rho_0 = 10^3$ kg m⁻³, and an arbitrary offset chosen such as to roughly match observed potential densities. The circle indicates the location of Ψ_B , the maximum streamfunction evaluated at 19°S; the plus indicates the location of Ψ_C , the maximum streamfunction evaluated at 49°S.

components of the streamfunction to the surface boundary conditions and the stratification in the basin to the north.

Specifically, we consider the isopycnal average along a given isopycnal path b between the outcrop latitude y_O , where the isopycnal intersects with the bottom of the surface layer (defined here as the minimum buoyancy at the uppermost model level), and the northern end of the channel $y_C = 49$ °S; that is,

$$\langle \Psi \rangle \equiv \frac{\int_{y_O}^{y_C} \Psi(y, b) \, dy}{l_C},\tag{6}$$

where $l_C = y_C - y_O$. Averaging Eq. (3) then yields

$$\langle \Psi \rangle = \langle \Psi^{\text{EU}} \rangle + \langle \Psi^{\text{GM}} \rangle + \langle \Psi^{\text{ST}} \rangle. \tag{7}$$

Given the definition of v_{GM} and assuming K to be constant, we can approximate the GM streamfunction as

$$\langle \Psi^{\rm GM} \rangle = \frac{K}{l_C} \int_{y_C}^{y_C} \frac{\partial \overline{[z]}}{\partial y} \bigg|_{b} w(y) \, dy \approx -KS_C W,$$
 (8)

with w(y) being the zonal width of the channel at latitude y. Neglecting variations in w(y), we approximate $w(y) \approx W$, where W is the characteristic zonal width of the channel. $S_C \equiv h_C/l_C > 0$ is the magnitude of the averaged slope of the isopycnal b in the channel, with $h_C > 0$ the difference between the depths of b at y_C and y_O . If we assume that the Eulerian mean circulation in the channel is solely set by the wind-induced Ekman transport, we can approximate it as

$$\langle \Psi^{\rm EU} \rangle \approx \frac{-1}{l_C} \int_{y_O}^{y_C} \frac{\tau}{\rho f} w(y) \, dy \approx -\left\langle \frac{\tau}{\rho f} \right\rangle W,$$
 (9)

with τ the wind stress, ρ the reference density, and f the Coriolis parameter. Following INM, we first neglect the effect of zonal asymmetry and $\langle \Psi^{ST} \rangle$ in which case Eq. (7) becomes

$$\langle \Psi \rangle \approx -\left\langle \frac{\tau}{\rho f} \right\rangle W - KS_C W.$$
 (10)

Equation (10) highlights the two external parameters, the wind stress strength τ and the GM diffusivity K, which characterize the two most important dynamical processes that control the overturning in the channel.

Equation (10) also depends on the channel-averaged isopycnal slope S_C , which remains to be constrained. Slope S_C is controlled by the surface boundary conditions and the stratification in the basin to the north, which in turn can be related to the basin buoyancy budget. Specifically, although INM adopted different assumptions for the specifics of the basin buoyancy budget, they all assumed an advective—diffusive balance, and, for scaling purposes, they can all be cast in the general form,

$$\Psi \sim -\kappa \frac{l}{h} W, \tag{11}$$

where κ is the vertical diapycnal diffusivity, l and h are horizontal and vertical length scales, with h characterizing the

TABLE 1. A summary of the notation used for different streamfunction components and overturning strengths.

Notation		Defined in
Ψ^{\dagger}	Isopycnal streamfunction	Section 2a
Ψ	Residual streamfunction	Section 2a
Ψ^{EU}	Eulerian mean streamfunction	Section 2a
$\Psi^{ m GM}$	GM streamfunction	Section 2a
$\Psi^{ ext{ST}}$	Stationary eddy streamfunction	Section 2a
$\langle \Psi angle$	Residual streamfunction averaged in the channel	Section 2b
Ψ_B	Max residual streamfunction at 19°S (within the basin)	Section 3c
Ψ_C	Max residual streamfunction at 49°S (channel-basin interface)	Section 3c

TABLE 2. Summary of abyssal-cell scaling theories based on the dynamics in the channel. We note that Mashayek et al. (2015) proposed a second scaling to apply above the abyssal boundary layer, which depends on the e-folding depth scale of diapycnal diffusivity. This scaling is not included here because we are not considering the effect of a vertically varying diffusivity. As defined in the main text, κ is the diapycnal diffusivity, K is the GM diffusivity, K is the width of the channel, τ_0 is the strength of wind stress, ρ is the reference density, and f is the Coriolis parameter. The dimensionless factor d encapsulates differing assumptions among these existing scaling theories (see the text).

	Proposed scaling	Description	Equivalent d
Ito and Marshall (2008)	$\Psi \sim -\sqrt{\kappa K \alpha} W$	Eq. (17) therein; applies to the limit where $ \Psi^{\mathrm{EU}} \ll \Psi^{\mathrm{GM}} $	$d = \alpha$
		(α is the ratio of isopycnal slope s and $z_0/L_{\rm ABL}$; z_0 is the characteristic depth scale of stratification; $L_{\rm ABL}$ is the meridional distance between the channel–basin interface and the latitude where the isopycnal incrops)	
Nikurashin and Vallis (2011)	$\Psi \sim \kappa K \frac{L_B}{L_C} \left(\frac{\tau_0}{\rho f}\right)^{-1} W$	Eq. (2.24) therein; applies to the limit where $ \Psi \ll \Psi^{EU} \approx \Psi^{GM} $	$d = \frac{L_B}{L_C}$
	$\Psi \sim -\sqrt{\kappa K \frac{L_B}{L_C}} W$	Eq. (2.32) therein; applies to the limit where $ \Psi \ll \Psi^{EU} \ll \Psi^{GM} $	
		$(L_B$ is the meridional length of the basin; L_C is the meridional length of the channel)	
Mashayek et al. (2015)	$\Psi \sim -\sqrt{\kappa K \frac{L_{\mathrm{ABL}}}{L_{C}}} W$	Eq. (13) therein; applies to the limit where $ \Psi^{EU} \!\ll \Psi^{GM} $	$d = \frac{L_{\text{ABL}}}{L_C}$
The general form	$\Psi \sim \kappa K d \left\langle \frac{\tau}{\rho f} \right\rangle^{-1} W$	Eq. (16) herein; applies to the limit where $ \Psi \ll \Psi^{EU} \approx \Psi^{GM} $	
	$\Psi \sim -\sqrt{\kappa K d} W$	Eq. (18) herein; applies to the limit where $ \Psi^{EU} \!\ll \Psi^{GM} $	
		(<i>d</i> is the ratio of channel-averaged isopycnal slope and an aspect ratio characterizing the basin advective–diffusive balance)	

vertical stratification and lW being the area of diffusive upwelling. Equation (11) suggests that Ψ within the basin is controlled by an aspect ratio, h/l, while the overturning in the channel is controlled by a different aspect ratio $S_C = h_C/l_C$ in Eq. (10). None of the variables, h_C , l_C , h, and l, are necessarily known a priori and different assumptions are made in the different theories. Nevertheless, we can generally rewrite Eq. (11) as

$$\Psi \sim -\kappa S_C^{-1} dW, \tag{12}$$

with $d \equiv S_C(h/l) = h_C l/(h l_C) > 0$ a dimensionless factor. The Ψ in Eq. (12) is most directly related to the transport into the basin, that is, the streamfunction evaluated at the channel-basin interface (i.e., $y = y_C$). Assuming that this quantity is well approximated by $\langle \Psi \rangle$ evaluated at the same buoyancy (an approximation that holds perfectly if the circulation is adiabatic in the channel), we can simultaneously solve Eqs. (10) and (12) to get ¹

$$\Psi = \langle \Psi \rangle \approx \frac{W}{2} \left(-\left\langle \frac{\tau}{\rho f} \right\rangle - \sqrt{\left\langle \frac{\tau}{\rho f} \right\rangle^2 + 4\kappa K d} \right). \tag{13}$$

Equation (13) is a generalized expression for Ψ in the channel and now becomes a function of three external parameters, τ , κ , and K, as well as the unknown parameter d.

The scaling relations derived by INM can be obtained by considering two specific limits of Eq. (13). To illustrate these limit cases, we can rewrite Eq. (13) as

$$\Psi \approx -\frac{W}{2} \left\langle \frac{\tau}{\rho f} \right\rangle (1 - \sqrt{1 + \varepsilon}), \tag{14}$$

where

$$\varepsilon \equiv \frac{4\kappa Kd}{\left\langle \frac{\tau}{\rho f} \right\rangle^2} \tag{15}$$

is a positive-definite nondimensional parameter [that is analog to Eq. (16) in Ito and Marshall (2008) and Eq. (2.23) in Nikurashin and Vallis (2011)], and we note that $\langle \tau(\rho f)^{-1} \rangle < 0$. In the limit $\varepsilon \ll 1$, Eq. (14) implies a scaling:

$$\Psi \sim \kappa K d \left\langle \frac{\tau}{\rho f} \right\rangle^{-1} W. \tag{16}$$

Equation (16) is identical to one of the scaling relations derived by Nikurashin and Vallis (2011) (with additional assumptions on d to recover their specific definition described in Table 2), and this limit case is equivalent to assuming

 $^{^{1}}$ We have omitted the positive solution because it corresponds to h < 0.

$$\langle \Psi^{\rm EU} \rangle \approx -\langle \Psi^{\rm GM} \rangle$$
 (17)

in Eq. (10); that is, the residual circulation is small relative to the wind- and eddy-driven circulations. On the other hand, if we consider the limit $\varepsilon \gg 1$ in Eq. (14), we obtain an alternative scaling,

$$\Psi \sim -\sqrt{\kappa K d} W, \tag{18}$$

which represents the common form of the scaling relations derived in INM (again with additional assumptions on d described in Table 2). The limit case considered in Eq. (18) is equivalent to assuming that the wind-driven circulation is negligible and thus

$$\langle \Psi \rangle \approx \langle \Psi^{\rm GM} \rangle$$
. (19)

Therefore, the two scaling predictions, Eqs. (16) and (18), can be regarded as applying to two different limits for the dominant balance in Eq. (10) [or more generally Eq. (7)].

It is important to note that for these scaling predictions to be closed, one has to further assume d to be relatively insensitive to the external parameters. Only then is Ψ solely a function of κ , K, and (depending on the considered limit case) τ , as suggested by INM, who made different assumptions to constrain $d \equiv S_C/(h/l) = h_C l/(h l_C)$. For a thorough comparison between INM, we have listed the implied assumption for d for each scaling theory in Table 2. As will be shown below, d, as defined here, is found to vary with various external parameters in our simulations, which turns out to be a major limiting factor for the predictive skill of these theories.

c. Scaling relations based on basin dynamics

Unlike INM, the scaling relation for Ψ derived by JN16 does not consider the dynamics in the channel but rather focuses on the dynamics in the basin. In the channel Ψ^{GM} is of leading-order importance in Eq. (3), due to the sloping isopycnals. For the basin, JN16 instead assumed that the isopycnals can be regarded as mostly horizontal so that Ψ^{GM} is small relative to $\Psi^{EU}.$ Retaining the assumption of a negligible contribution by the stationary eddy streamfunction, i.e., $\Psi^{ST},$ Eq. (3) in the basin is then reduced to

$$\Psi \approx \Psi^{EU}$$
. (20)

The Ekman transport can also be assumed to be negligible in the abyssal basin so that the circulation is in geostrophic balance. Thermal wind balance then suggests

$$f \frac{\Psi^{\rm EU}}{h_x^2} \sim \Delta b_x, \tag{21}$$

that is, the Eulerian mean streamfunction is determined by a depth scale h_x , characterizing the vertical scale over which $\Psi^{\rm EU}$ increases from zero to its maximum value, and the zonal buoyancy contrast across the basin Δb_x . The subscript x here is used to denote the scales relating to the thermal wind scaling.

Combining Eqs. (20) and (21) with the basin thermodynamic scaling, Eq. (11), and defining a dimensionless factor, $d_1 = h_x/h$, as the ratio of the two depth scales therein, one derives

$$\Psi \sim \left(\frac{\kappa^2 l^2 W^2 \Delta b_x d_1^2}{f}\right)^{1/3}.$$
 (22)

Equation (22) is not a closed expression because l, Δb_x , and d_1 are left to be determined. Applying Eq. (22) to the abyssal boundary layer (ABL), JN16 assume l to be the meridional extent of the ABL and to scale with the basin length (L_B) and diagnosed Δb_x as the meridional buoyancy contrast averaged over the ABL from the simulations. [While it is the zonal buoyancy contrast that is of relevance in the thermal wind balance in Eq. (21), JN16 assumed the zonal and meridional buoyancy contrasts in the ABL to scale with one another]. With these working definitions and assuming d_1 to be constant, they found that Eq. (22) explains the sensitivity of the basin streamfunction maximum in their simulations to the surface buoyancy loss integrated over the Southern Ocean deep water formation region, B (cf. their Fig. 9). Since B does not directly appear in Eq. (22), the sensitivity to B is captured implicitly by the change of Δb_x with B.

To explicitly express Eq. (22) in terms of B, we need to eliminate Δb_x in Eq. (22) with another scaling relating Δb_x and B. More readily, the buoyancy flux can be related to the bulk buoyancy contrast across the abyssal cell,

$$\Delta b_B \equiv B_B \Psi^{-1} \sim B \Psi^{-1} \,, \tag{23}$$

where B_B is the net meridional buoyancy transport by the abyssal cell at the latitude where Ψ is evaluated. Assuming that the net buoyancy gain by the abyssal cell south of this latitude is relatively small (or amounts to an approximately constant fraction of B), we expect B_B to be proportional to the surface buoyancy loss in the bottom water formation region, B. Introducing another dimensionless factor, $d_2 \equiv \Delta b_x/\Delta b_B$, we can then combine Eqs. (22) and (23) to get

$$\Delta b_B \sim \left(\frac{B^3 f}{\kappa^2 l^2 W^2 d_1^2 d_2}\right)^{1/4} \quad \text{and} \tag{24}$$

$$\Psi \sim \left(\frac{B\kappa^2 l^2 W^2 d_1^2 d_2}{f}\right)^{1/4},\tag{25}$$

which now directly predict the bulk buoyancy contrast and the streamfunction's dependence on B. Equation (25) is a closed expression for the strength of the overturning if the length scale l, as well as the dimensionless factors d_1 and d_2 , can be assumed constant.

While JN16 did not explicitly test Eq. (25), their simulations are seen to nicely follow Eq. (25). In JN16's Fig. 9, the simulated streamfunction maximum varies between 2.5 and 4 Sv over a factor-of-6 change in the prescribed buoyancy loss rate, giving a power-law scaling $\propto B^{0.26}$, which is almost indistinguishable from the prediction of Eq. (25) that $\Psi \propto B^{1/4}$ and therefore numerically supports the scaling argument.

From the above derivations, it becomes clear that the basinbased scaling, Eq. (25), predicts a very different parameter dependence from the channel-based scalings in Eqs. (16) and (18), and indeed is derived from very different dynamics. To better understand how the two sets of theories may be reconciled, we conduct a set of idealized model simulations, which are described in the next section.

3. Model and diagnostics

a. Model configuration

We run our numerical simulations using the hydrostatic Boussinesq version of the Massachusetts Institute of Technology General Circulation Model (Marshall et al. 1997). The model geometry and resolution are as in JN16. That is, we have a basin spanning from 0° to 60° E and from 69° N to 48° S. Attached on its south side is a zonally periodic channel extending to 69° S. The horizontal resolution is one degree. The full depth of the model is $H = 4 \, \text{km}$, modeled with 28 levels with varying vertical resolution.

We use a linear equation of state, with a single buoyancy variable, b, which can be interpreted only in a relative sense. Throughout the domain, we apply a spatially uniform vertical diapycnal diffusivity $\kappa = 6 \times 10^{-5} \, \mathrm{m^2 \, s^{-1}}$. For the parameterized mesoscale eddy transport, we use the GM parameterization with the transfer coefficient chosen as $K = 700 \, \mathrm{m^2 \, s^{-1}}$.

Our boundary conditions are designed with the intention to omit the processes not central to the existing theoretical arguments and to simulate only the abyssal overturning cell. For the bathymetry, we first consider a flat bottom boundary. The effects of bottom topography will then be discussed in section 5 separately. For the wind stress, we choose the simple form

$$\tau(y) = \begin{cases} 0 & \text{for } y > y_C \\ \tau_0 \sin\left(\pi \frac{(y - y_S)}{(y_C - y_S)}\right) & \text{for } y \le y_C \end{cases},$$

where $y_C = 49^{\circ}\text{S}$ and $y_S = 69^{\circ}\text{S}$ are the latitudes of the channel-basin interface and the southern end of the channel, respectively. This ensures the wind stress is maximized with its magnitude $\tau_0 = 0.2\,\text{N m}^{-2}$ at the midchannel and vanishes at the channel-basin interface, thus effectively eliminating any direct effect of the continent on the wind-driven circulation in the channel.

Surface buoyancy forcing F_b is applied as

$$F_b(y) = \begin{cases} R(b-b_R) & \text{for} \quad y > y_C \\ 0 & \text{for} \quad y_I < y \leq y_C \\ B/A_I & \text{for} \quad y \leq y_I \end{cases}.$$

In the basin, we use a restoring boundary condition with the restoring strength, R, equivalent to an adjustment time scale of 3 months for the 50-m-deep top model layer, and a constant reference buoyancy, b_R . This results in surface fluxes over the basin being close to horizontally uniform in the simulations. In the channel, we prescribe buoyancy forcing only south of a prescribed latitude, which we interpret as the effective sea ice line, $y_I = 60^{\circ}$ S. South of the sea ice line, we prescribe an integrated surface buoyancy loss, B, uniformly distributed over the enclosed area, A_I (between y_S and y_I), which amounts to a surface buoyancy loss rate per unit area, $B/A_I = 2 \times 10^{-9} \,\mathrm{m}^2 \,\mathrm{s}^{-3}$. North of $y_I = 60^{\circ}$ S in the channel, we impose a no-flux boundary condition, which effectively eliminates the presence of an upper (clockwise)

overturning cell, which does not appear in the theories discussed in section 2. The choice to exclude the upper cell therefore aligns with our intention to include only the essential processes that enter in the existing theories, and is consistent with the approach taken by Nikurashin and Vallis (2011) and Mashayek et al. (2015).

To study the parameter dependence predicted by the theories discussed in section 2, we perform a set of sensitivity simulations. We vary one of the following parameters at a time, with their control values as described above: the prescribed surface buoyancy loss B, the diapycnal diffusivity κ , the latitude extent of the prescribed buoyancy loss ($\delta_I \equiv y_I - y_S$; with fixed B), the magnitude of the prescribed wind stress τ_0 , and the GM diffusivity K. We integrate each simulation to a statistically steady state, and all diagnostics are computed using the model output from the last 50 years.

b. Overturning circulation in the control simulation

The meridional overturning circulation in our control simulation, measured via the isopycnal streamfunction, $\Psi^{\dagger}(y, b)$ [defined in Eq. (1)], and the residual streamfunction, $\Psi(y, z)$ [defined in Eq. (2)], is shown in Fig. 1. A single well-defined anticlockwise overturning circulation is seen, which is an idealized representation of the abyssal overturning cell. The surface water, exposed to the prescribed buoyancy loss in the southern part of the channel, sinks along the sloping isopycnals in the channel until reaching the bottom of the ocean near the channel-basin interface. This "Antarctic Bottom Water" flows northward into the basin, forming the lower branch of the cell in the basin, and upwells within the basin where it encounters diapycnal diffusion and gains buoyancy as the abyssal stratification decreases toward and vanishes at the bottom, i.e., $\partial_z(\kappa \partial_z b) > 0$. The upwelled water then moves southward in the upper branch of the cell at middepth and is divided into two routes. In one route the water loses buoyancy via diapycnal mixing due to the bottom-intensified stratification near the southern end of the basin, i.e., $\partial_z(\kappa \partial_z b) < 0$, and thus recirculates back into the abyssal basin. In the other route, the water continues to upwell along the isopycnals in the channel back to the surface and closes the overturning loop.

c. Diagnostic metrics for the overturning strength

Because of the recirculation near the channel-basin interface, the global maximum Ψ (in terms of the absolute value) is seen to locate within the southern part of the basin in our simulations. Such an appearance of the maximum streamfunction within the basin can also be seen in other idealized model simulations (e.g., JN16; Jones and Abernathey 2019) as well as in an ocean state estimate (e.g., Cessi 2019). JN16 apply their scaling relations to explain this streamfunction maximum in the southern part of the basin. On the other hand, as discussed in section 2, the scaling theories of INM are better interpreted as explaining Ψ in the channel or at the channelbasin interface. To account for the difference between JN16 and INM and to compare the model results with both theories, we explicitly consider two diagnostic metrics, with one measuring the overturning strength within the basin and the other measuring the overturning strength within the channel (Fig. 1). The characteristic basin overturning strength, Ψ_B , is evaluated

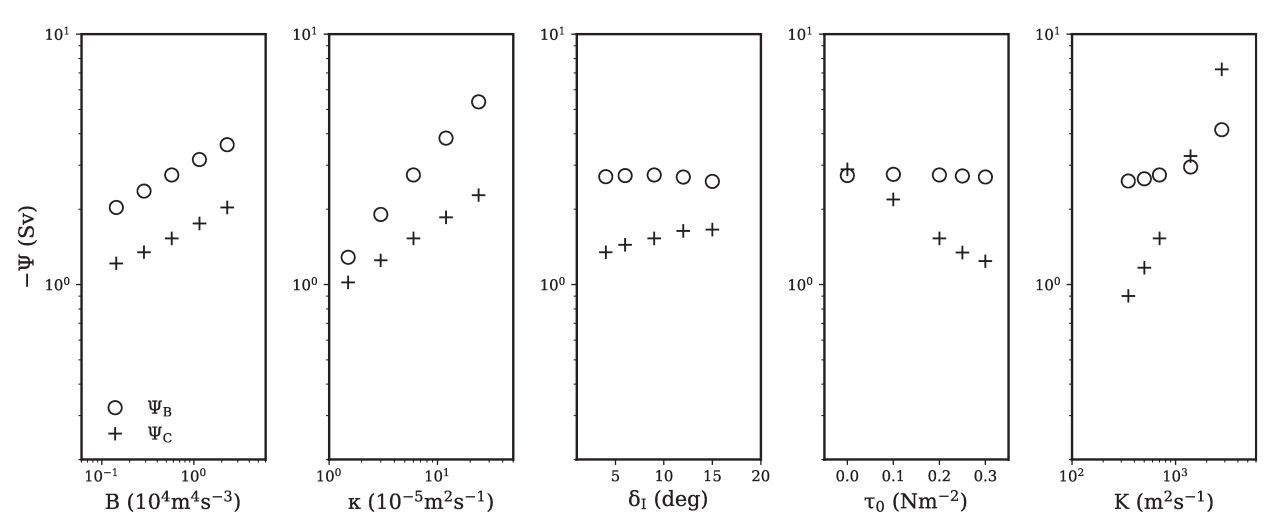


FIG. 2. The overturning strength in the basin (Ψ_B ; circles) and in the channel (Ψ_C ; plus signs) as a function of the external parameters: (left) the rate of surface buoyancy loss B, (left center) diapycnal diffusivity κ , (center) the latitudinal extent of surface buoyancy loss δ_I , (right center) the strength of the wind stress τ_0 , and (right) the GM diffusivity K.

as the maximum Ψ at 19°S (i.e., the latitude of the global maximum in the control simulation). The characteristic channel overturning strength, Ψ_C , is evaluated as the maximum Ψ at 49°S (i.e., the latitude of the channel–basin interface).

The diagnosed Ψ_B and Ψ_C are shown as a function of the external parameters in Fig. 2. It is clearly seen that Ψ_B and Ψ_C , representing the different measures of the overturning strength in the basin and in the channel, respectively, differ substantially in their dependence on the external parameters. This implies that JN16 and INM in fact consider the overturning strengths in different parts of the abyssal cell, which may partially explain the apparent contradiction in the scaling theories they proposed. In the next section, we test the scaling theories for Ψ_C and Ψ_B separately to illustrate the distinct dynamics controlling them.

4. Theory-simulation comparison

a. Overturning strength in the channel

We first examine the extent to which Ψ_C , the maximum Ψ evaluated at the channel–basin interface, can be predicted by the scaling theories of INM that are based on the channel dynamics, i.e., Eqs. (16) and (18). Recall that these two scaling relations are obtained by considering two approximations, Eqs. (17) and (19), respectively. Since they characterize the relative importance of the different components in Eq. (7), we start by comparing these terms to decide which limit case better describes our simulations. We first confirm that Ψ_C is indeed qualitatively similar to the isopycnally averaged streamfunction in the channel, i.e., $\Psi_C \approx \langle \Psi \rangle$ (Fig. 3). The decomposition of $\langle \Psi \rangle$ into $\langle \Psi^{\rm EU} \rangle$ and $\langle \Psi^{\rm GM} \rangle$ according to Eq. (7) is then shown in

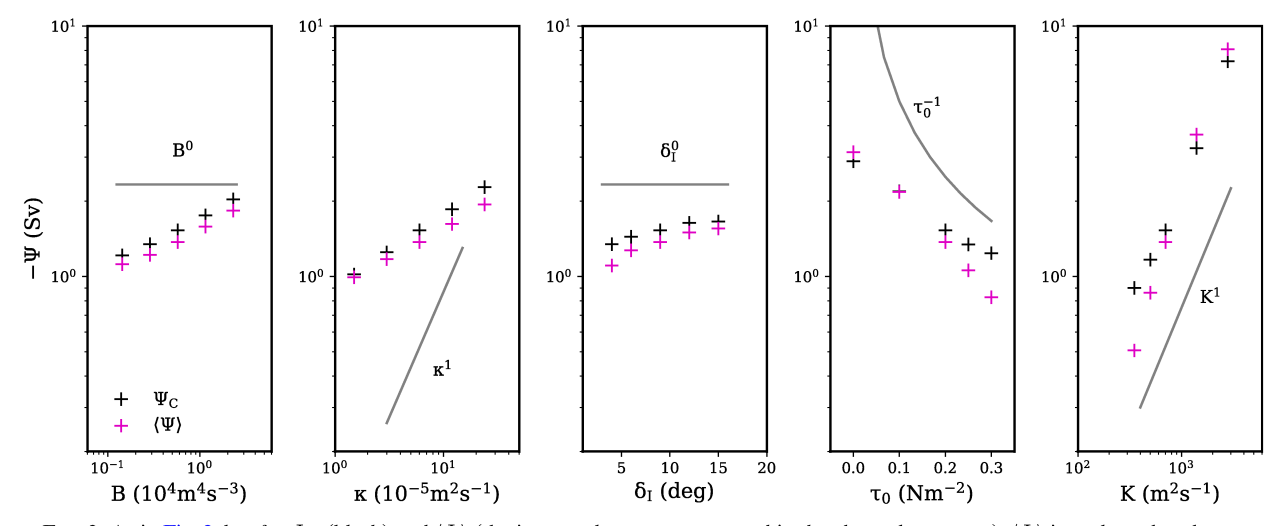


FIG. 3. As in Fig. 2, but for Ψ_C (black) and $\langle \Psi \rangle$ (the isopycnal average computed in the channel; magenta); $\langle \Psi \rangle$ is evaluated at the same buoyancy as Ψ_C , i.e., the buoyancy at which the circulation at the channel–basin interface obtains its maximum. The lines indicate the power-law scaling predicted by Eq. (16). Notice that the x axis is linear in the fourth panel, because we are including a case with zero wind stress.

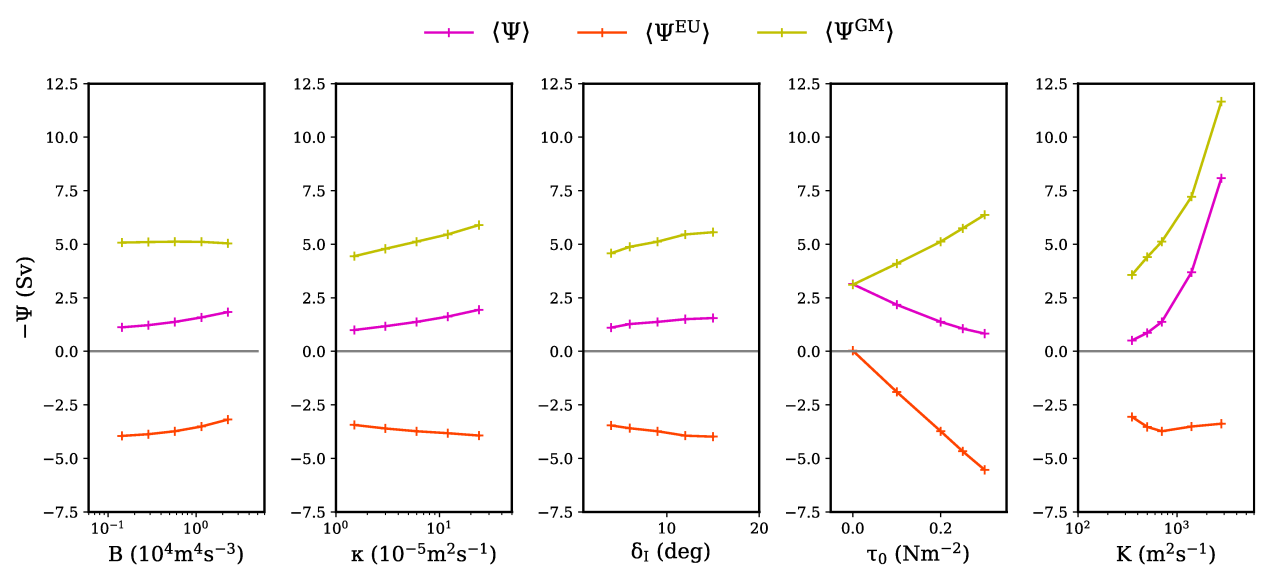


FIG. 4. Decomposition of the channel-averaged streamfunction $\langle \Psi \rangle$, based on Eq. (7). Notice that the sign of all streamfunction components is reversed, and $\langle \Psi^{ST} \rangle$ is not shown because it is virtually zero in all cases.

Fig. 4. In general, we find the dominant balance to be between $\langle \Psi^{EU} \rangle$ and $\langle \Psi^{GM} \rangle$. The two substantially cancel each other and result in a relatively small $\langle \Psi \rangle$. Therefore, we expect that $\langle \Psi \rangle$ is better predicted by Eq. (16) than Eq. (18).

Equation (16) does qualitatively explain the increase of $\langle \Psi \rangle$ with increasing κ , increasing K, and decreasing τ_0 , but it generally fails to predict the correct power-law dependence on these external parameters (Fig. 3). In some cases, such as when τ_0 decreases to zero and $\langle \Psi^{EU} \rangle$ vanishes, the failure of Eq. (16) can be partially attributed to the breakdown of the approximation in Eq. (17), such that the fit may be improved by considering the generalized solution, Eq. (13).

However, we find that perhaps the most fundamental limitation in the channel scaling theories is that the dimensionless factor $d = (S_C)/(h/l)$ in Eq. (13) also varies with the external parameters. In Fig. 5, we plot S_C (the numerator of d) against h/l (the denominator of d), with all quantities diagnosed from the simulations. It is found that h/l shows substantial parameter dependence, while S_C varies comparatively little (presumably due to geometrical constraints). As a result, the ratio, d, varies systematically with κ , τ_0 , and K. Although less strongly, d also depends on B and δ_I , which indeed is essential to explain the dependence of $\langle \Psi \rangle$ on B and δ_I , which do not appear explicitly in Eq. (13). A quantitative improvement on the existing theories therefore requires a theory for how d depends on the external parameters, which remains missing.

b. Overturning strength in the basin

We now consider the overturning circulation in the basin Ψ_B , which we find to be more readily explained by the theoretical prediction than the channel circulation discussed above. The scaling prediction for the residual streamfunction in the basin is described by Eq. (25), which suggests that Ψ_B scales as $B^{1/4}\kappa^{1/2}$. This predicted parameter dependence is seen to agree with most of our simulations (Fig. 6). For our varying B cases,

we see a $B^{1/4}$ dependence; for our varying δ_I but fixed B cases, we see no dependence on δ_I . In addition, we see that Ψ_B scales as $\kappa^{1/2}$ but stays approximately constant when τ_0 is varied. If B and κ are varied together, the predicted $B^{1/4}\kappa^{1/2}$ dependence also remains valid (not shown). These results all provide supporting evidence for Eq. (25). An apparent exception appears when K is large. In this limit, changes in the GM streamfunction in the basin become nonnegligible, such that Eq. (20) as an underlying assumption behind Eq. (25) no longer holds.

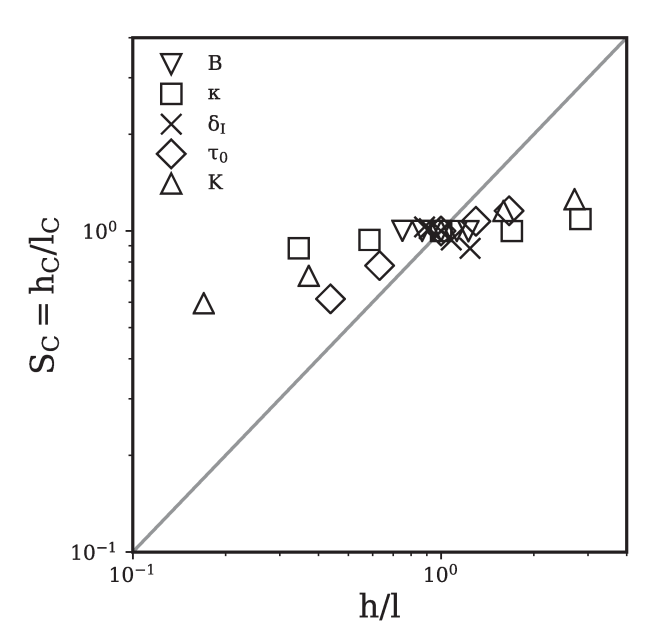


FIG. 5. Evaluating changes in $d = S_C/(h/l)$: $S_C = h_C l_C$ is plotted against h/l. The latter is calculated as $h/l = -\kappa W \langle \Psi \rangle^{-1}$ such that Eq. (11) holds perfectly. All values are normalized by the corresponding values in the control simulation.

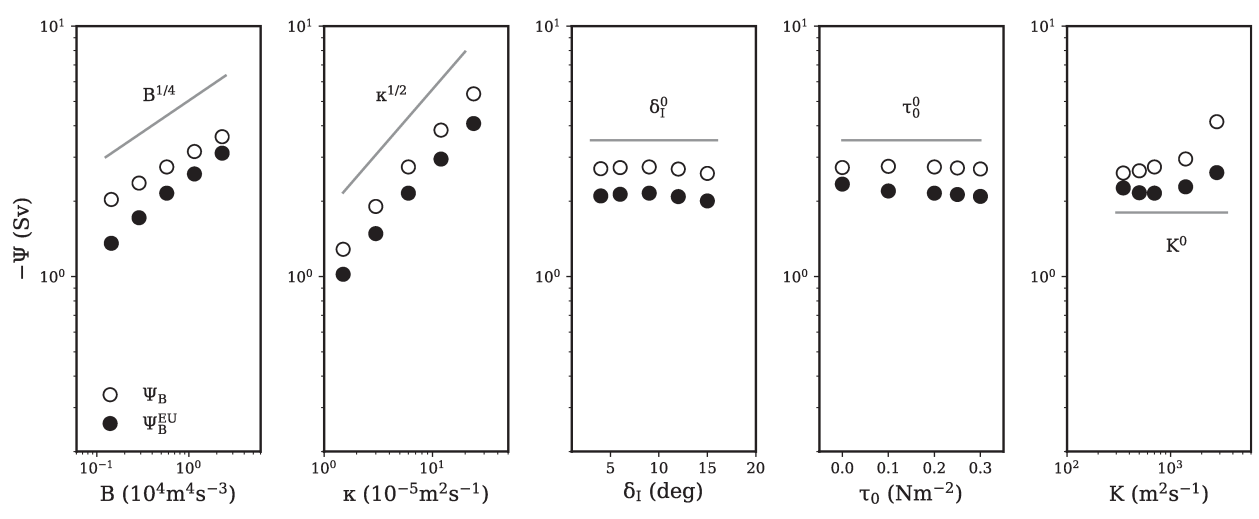


FIG. 6. As in Fig. 2, but for Ψ_B (the maximum residual streamfunction evaluated at 19°S) and $\Psi_B^{\rm EU}$ (the maximum Eulerian mean streamfunction evaluated at 19°S). The lines indicate the power-law scaling predicted by Eq. (25).

This interpretation is supported by the increasing differences between the maximum residual streamfunction, Ψ_B , and the maximum Eulerian mean streamfunction $\Psi_B^{\rm EU}$, shown in Fig. 6.

The above analysis focuses on the maximum value of the residual streamfunction, Ψ_B , but the same scaling argument also has skill in predicting the vertical profile in buoyancy space. In Fig. 7, we plot the simulated profiles of Ψ evaluated at 19°S as a function of the buoyancy difference, $\Delta b = b - b_B$, where b_B is the buoyancy where the streamfunction obtains its maximum value (i.e., Ψ_B). The streamfunction on the x axis is normalized according to the predicted maximum in Eq. (25) and the buoyancy difference on the y axis is normalized according to the predicted buoyancy

contrast in Eq. (24). Figure 7 shows that, except for the simulations with large K, the results collapse reasonably well on each other. While some nonnegligible deviations exist, the scaling argument therefore provides a useful description for not only the maximum value but also the overall shape of $\Psi(b)$.

We caution, however, that there are in fact some subtleties in the derivation of Eq. (25), which may put into question the generality of this scaling relation. Specifically, although Eq. (25) successfully predicts the parameter dependence of the basin overturning strength in our simulations, the dimensionless factors d_1 and d_2 , in Eq. (25) do exhibit nontrivial sensitivity to the external parameters (see the appendix). However, $d_1^2d_2$ stays mostly unchanged within

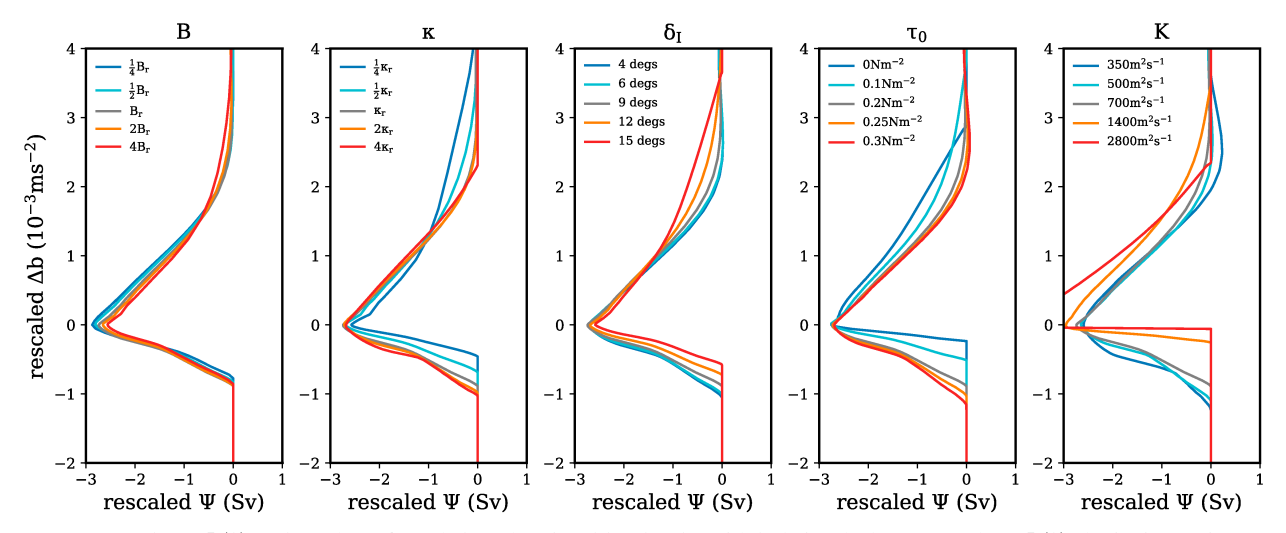


FIG. 7. Profiles of $\Psi(b)$ evaluated at 19°S and plotted against $\Delta b = b - b_B$, with b_B being the buoyancy where $\Psi(b)$ obtains its maximum. Both Ψ and Δb are rescaled to account for the predicted stretching and amplifying effect due to the parameter changes. Specifically, Δb is normalized by $(B/B_r)^{3/4}(\kappa/\kappa_r)^{-1/2}$ according to Eq. (24), and Ψ is normalized by $(B/B_r)^{1/4}(\kappa/\kappa_r)^{1/2}$ according to Eq. (25). The subscript r denotes the value obtained in the control simulation.

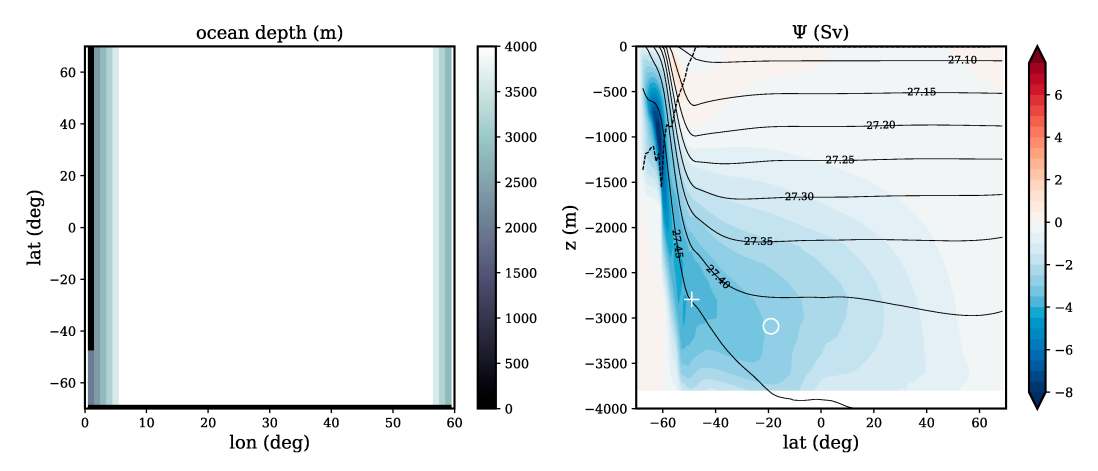


FIG. 8. Model setup and control-case results for the simulations with bottom topography: (left) the ocean depth and (right) $\Psi(y, z)$, with black lines indicating the zonally averaged depth of a given isopycnal in the control simulation. The dashed line indicates the bottom of the surface layer, defined as the mean depth of the isopycnal corresponding to the maximum surface density at a given latitude.

the parameter range we explored, allowing Eq. (25) to be a useful predictor.

5. Role of bottom topography

The simulations we examined so far have a flat bottom throughout the entire model domain, which eliminates potential effects associated with bottom topography in the Southern Ocean. To address the role of bottom topography, we compare our flat-bottom simulations with a new set of simulations where everything is kept the same except that the model is set up with an idealized bottom topography. That is, a topographical ridge is included, which extends the continent with a maximum height of 2 km throughout the entire channel. The exact form of the ridge is shown in Fig. 8 and is designed to be qualitatively similar to the model setup in Ito and Marshall (2008).

The overturning circulation in the control simulation is significantly affected by the presence of topography (cf. Fig. 8 to Fig. 1). The global maximum (in terms of absolute value) now appears in the channel rather than the basin. The effect of topography on the overturning strength depends strongly on where the circulation is evaluated. In Fig. 9, we compare the overturning strength between the flat-bottom and the topography simulations, across the full parameter range. As in the previous analysis, we show the two different diagnostic metrics, Ψ_B and Ψ_C , which measure the overturning strength in the basin and in the channel, respectively. Although the presence of the bottom ridge interferes with the circumpolar zonal flow in the lower portion of the channel, we retain our earlier definition of Ψ_C as the maximum streamfunction at 49°S, which again is reasonably similar to the isopycnally averaged streamfunction in the channel, $\langle \Psi \rangle$ (Fig. 10).

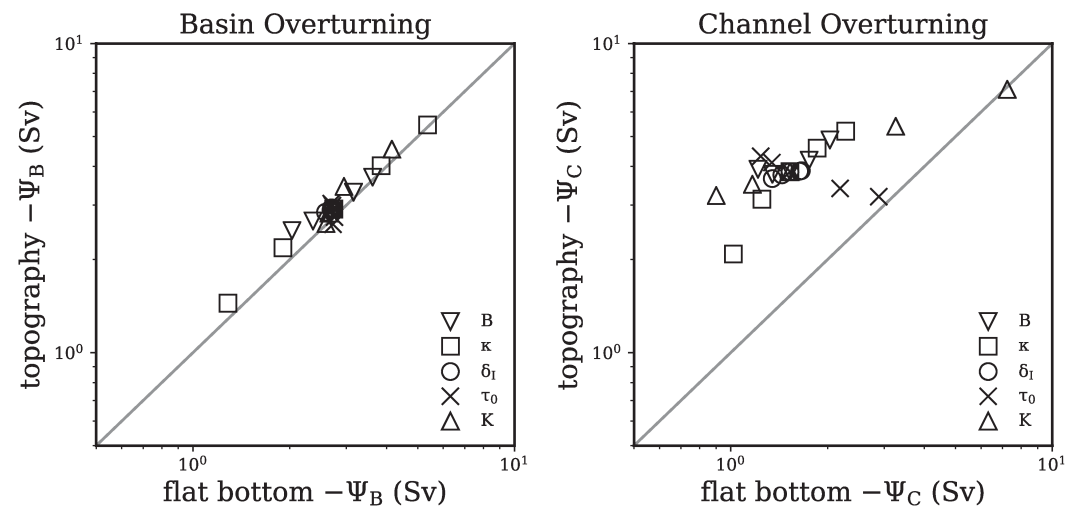


FIG. 9. Comparison of the overturning strength between the flat-bottom simulations and the simulations with bottom topography: (left) Ψ_B and (right) Ψ_C .

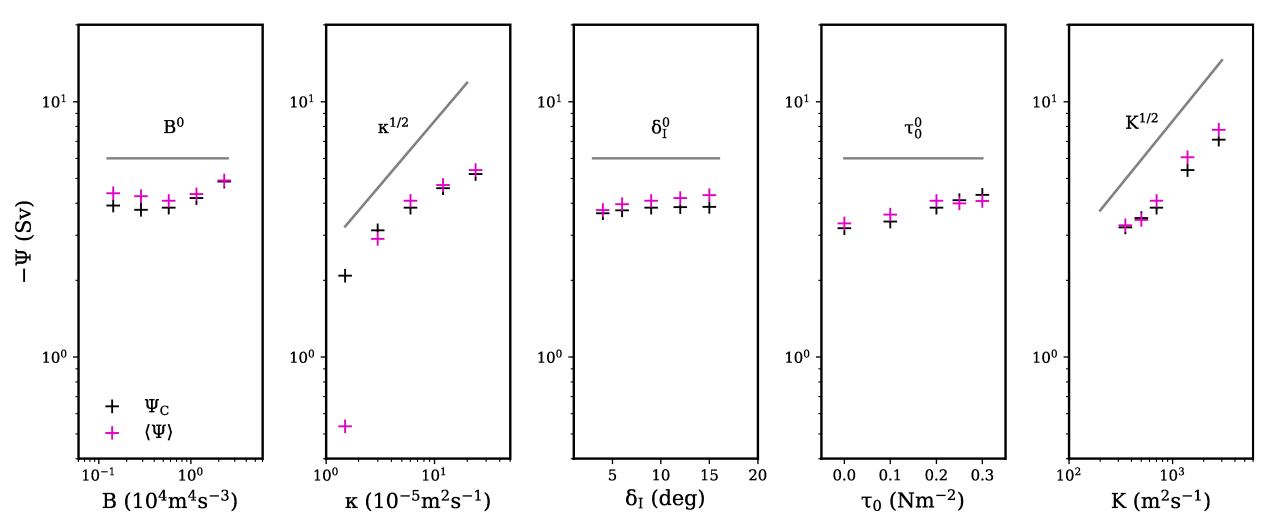


FIG. 10. As in Fig. 3, but for the simulations with bottom topography. The lines indicate the power-law scaling predicted by Eq. (18).

The Ψ_B in simulations with topography is only slightly larger than in the flat-bottom simulations; the two scale well with each other and have very similar parameter dependence (left panel in Fig. 9). This suggests that the presence of bottom topography in the channel has little impact on the dynamics controlling the overturning strength within the basin. It also reaffirms that the details of the channel dynamics, which are strongly affected by the bottom topography, may not be as crucial to understand the abyssal circulation in the basin.

On the contrary, the results for Ψ_C are substantially modified after the bottom topography is introduced (right panel in Fig. 9). The magnitude of Ψ_C in the topography simulations is generally much larger than in the flat-bottom simulations, and the two cases do not seem to scale well with each other.

A decomposition of the channel-averaged streamfunction $\langle \Psi \rangle$ reveals that the difference between the flat-bottom and topography simulations is in part due to the contribution by the stationary eddy streamfunction $\langle \Psi^{ST} \rangle$. In the topography simulations, stationary eddies contribute significantly to the total transport, owing to the presence of bottom topography that breaks the zonal symmetry in the channel. As shown in Fig. 11, $\langle \Psi^{ST} \rangle$ acts to approximately cancel $\langle \Psi^{EU} \rangle$. This almost perfect standing eddy compensation is especially important in explaining the much weaker τ_0 dependence of $\langle \Psi \rangle$ in the topography simulations (Fig. 11) relative to the flat-bottom simulations (Fig. 4). We note that a similar behavior is reported by Bishop et al. (2016), although the reasons for and robustness of this compensation remain unclear.

A direct result of the compensation between $\langle \Psi^{ST} \rangle$ and $\langle \Psi^{EU} \rangle$ is that $\langle \Psi \rangle$ is left to mostly follow $\langle \Psi^{GM} \rangle$, which makes Eq. (19) a decent approximation, albeit not for the reason assumed in the existing theories (i.e., $\langle \Psi^{ST} \rangle \approx \langle \Psi^{EU} \rangle \approx 0$). Moreover, we find that the dimensionless factor d is less sensitive to the external parameters in the simulations with bottom topography (not shown). Consequently, Eq. (18) more accurately predicts Ψ_C in these simulations (Fig. 10).

6. Conclusions

This study revisits existing theories for the abyssal overturning strength (Ito and Marshall 2008; Nikurashin and Vallis 2011; Mashayek et al. 2015; JN16), aiming to better interpret their apparent contradiction regarding the importance of channel versus basin dynamics. An ocean general circulation model is set up with idealized geometry and surface forcing conditions that encapsulate only the essential elements in these theories. Using this model, we conducted a series of sensitivity runs to study the parameter dependence of the circulation strength. The external parameters we varied are the integrated surface buoyancy loss rate prescribed in the channel B, the diapycnal diffusivity κ , the latitudinal extent of the prescribed buoyancy loss δ_I , the magnitude of the prescribed wind stress τ_0 , and the GM diffusivity K. Our key findings are summarized in the following:

- The strengths of the residual overturning circulation Ψ measured within the channel and within the basin can vary with the external parameters in distinct ways due to the possibility of a significant recirculation in the basin. Thus, the apparent inconsistency among the theories with different dynamical focuses can at least in part be explained by the fact that they are attempting to explain different measures of the circulation strength.
- Within the channel, Ψ is seen to depend on all parameters, B, κ , δ_I , τ_0 , and K in the simulations with a flat bottom. When a bottom ridge is included in the channel, Ψ is to-the-first-order only sensitive to κ and K, as predicted by the existing theories that consider channel dynamics [i.e., Eq. (18)]. This difference between the flat-bottom and topography simulations is due to the presence of stationary eddies in the latter, which effectively cancel the mean circulation, allowing the residual circulation to be well approximated by the parameterized eddy-driven circulation. This approximation reduces the complexity of the problem and is a key assumption in the INM theories. Why this almost perfect cancellation occurs, however, remains unclear.

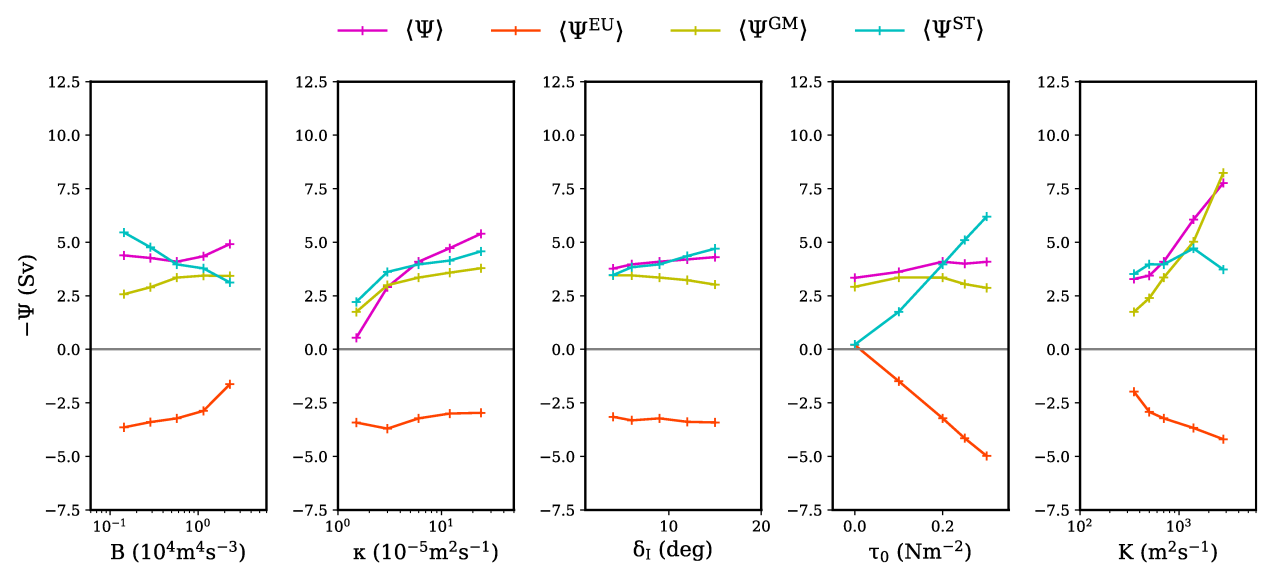


FIG. 11. As in Fig. 4, but for the simulations with bottom topography.

Within the basin, Ψ is found to scale with B^{1/4}κ^{1/2}, as described in Eq. (25). Building on the basin-based argument proposed by JN16, this scaling is derived without consideration of channel dynamics and is instead based on advective-diffusive balance and thermal wind relation in the basin. Consistent with the importance of basin over channel dynamics, the overturning strength in the basin is similar in simulations with and without channel topography.

Although the focus of this study is on the circulation strength, we note that the vertical extent of the overturning circulation, at the channel-basin interface and within the basin, are also seen to vary differently with the external parameters. This aspect of the circulation changes can be potentially important when considering the interaction with the upper (clockwise) cell. Since we have set up the model purposely to eliminate the upper cell, this is a subject that cannot be addressed in this study but may deserve a closer look in future work.

A related question is to what extent these theories for the abyssal overturning strength, which have been derived for and validated in single-basin models so far, also apply to multibasin and global models. Nadeau and Jansen (2020) recently showed that the general results for the global overturning circulation in a single-basin setup can be largely carried over to a two-basin setup after accounting for the domain size effects. While these results suggest that single-basin theories remain qualitatively relevant to models with more complicated geometries, in how far the scaling arguments discussed here would hold quantitatively requires more investigation.

In addition, the analyses we performed in this study are limited to the equilibrium response of the circulation changes. All theories we discussed make use of the basin thermodynamic scaling [i.e., Eq. (11)], which assumes the basin buoyancy budget to be in equilibrium. This assumption will need to be modified

when the storage term in the budget is nonnegligible—for example, as is expected during anthropogenic climate change in the coming decades.

Despite these remaining questions, we believe our results can provide useful insights that improve our understanding of the relative importance of different mechanisms in controlling the abyssal circulation. Particularly noteworthy is the importance of thermodynamics, specifically buoyancy forcing and diapycnal mixing, and the comparatively small role of wind stress in controlling the abyssal overturning in the basin as well as in the channel when topography is present. A better understanding of the processes that control buoyancy forcing around Antarctica and turbulent mixing in the abyss is thus crucial to better constrain and predict past and future changes in the abyssal overturning circulation.

Acknowledgments. Computational resources for this project were generously provided by the University of Chicago Research Computing Center. Authors Chang and Jansen acknowledge support from NSF Award OCE-1846821.

Data availability statement. The MITgcm configuration files used for this study are available online (https://github.com/cyinchang/MITgcm-abyss).

APPENDIX

Dimensionless Factors in Eq. (25)

Equation (25) predicts the parameter dependence of the basin overturning strength in terms of external parameters only if the combination of the dimensionless factors, $d_1^2d_2$, is independent of the external parameters. To verify this assumption, we have explicitly diagnosed $d_1 \equiv h_x/h$ and $d_2 \equiv \Delta b_x/\Delta b_B$ from our simulations. Specifically, based on Eq. (21) and loosely following JN16, we calculate h_x as the height of the maximum

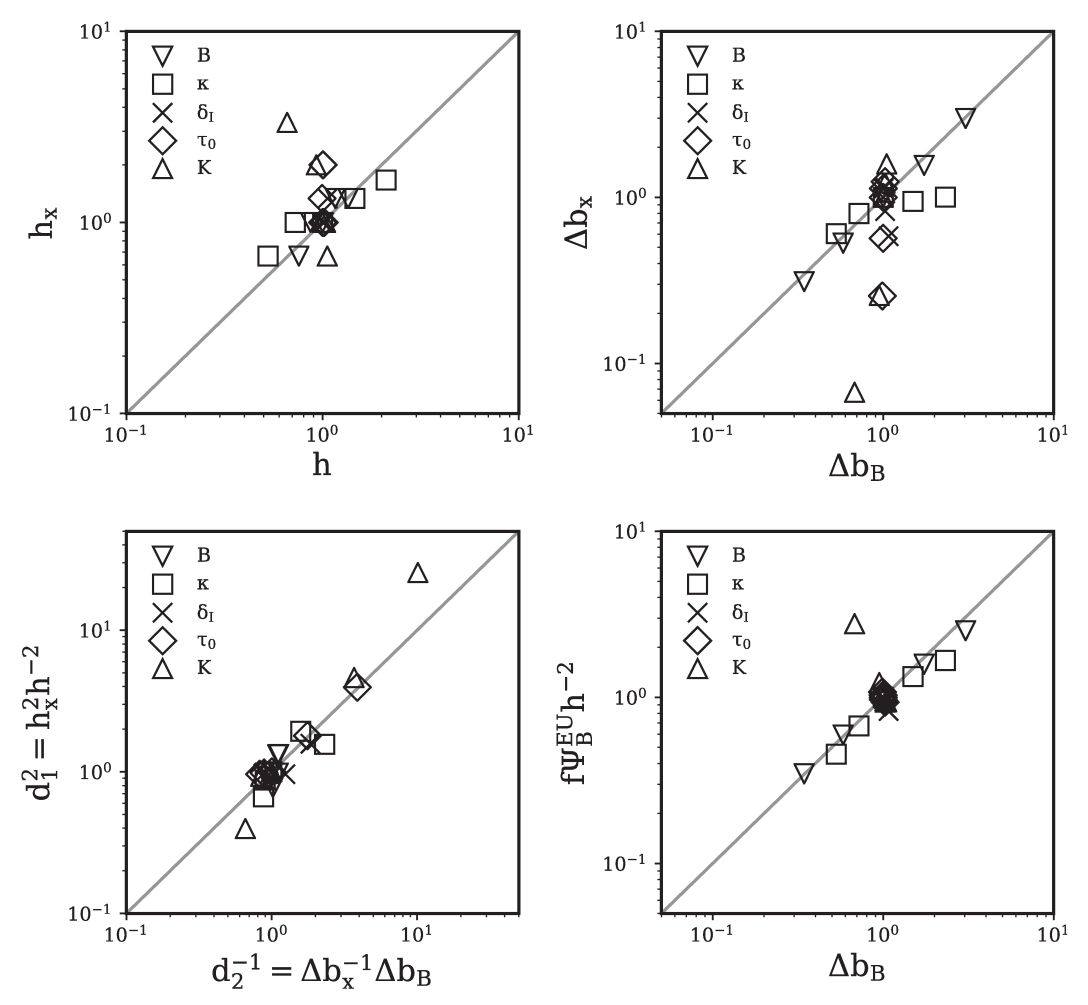


FIG. A1. (top left) The h_x plotted against h, (top right) Δb_x plotted against Δb_B , (bottom left) $d_1^2 = h_x^2 h^{-2}$ plotted against $d_2^{-1} = \Delta b_x^{-1} \Delta b_B$, and (bottom right) the lhs of Eq. (A1) plotted against the rhs. All results are normalized by the corresponding values in the flat-bottom control simulations.

Eulerian overturning Ψ_B^{EU} above the ocean bottom and Δb_x as the zonal buoyancy difference across the basin and averaged vertically between the bottom and the height of the streamfunction maximum. The definition for Δb_B is specified in Eq. (23). As in section 2, we compute h from Eq. (11), using the diagnosed Ψ_B and assuming $l=L_B$ to get an estimate of h.

The obtained results indicate that $d_1^2d_2$ is indeed mostly invariant in our simulations, although both d_1 and d_2 individually vary with the external parameters. As seen in Fig. A1, the variations in h_x (numerator of d_1) and h (denominator of d_1) do not generally scale with each other, so that d_1 is generally not constant. Similarly, Δb_x (numerator of d_2) and Δb_B (denominator of d_2) do not generally scale with each other, leading to variations in d_2 . However, d_1^2 scales reasonably well with d_2^{-1} , such that $d_1^2d_2$, which enters the scaling in Eq. (25), remains approximately constant.

An implication of the constancy of $d_1^2 d_2$ is that we can rewrite Eq. (21) as a modified thermal wind scaling,

$$f\frac{\Psi^{\rm EU}}{h^2} \sim \Delta b_B,\tag{A1}$$

which effectively replaces h_x and Δb_x with h and Δb_B in Eq. (21). Equation (A1) combined with Eqs. (11), (20), and (23) gives Eq. (25), but with the dependence on d_1 and d_2 eliminated. Although Eq. (A1) holds in our simulations, it remains unclear to us as to how far this relationship can be expected to be robust.

REFERENCES

Adkins, J. F., 2013: The role of deep ocean circulation in setting glacial climates. *Paleoceanography*, 28, 539–561, https://doi.org/ 10.1002/palo.20046.

Bishop, S. P., P. R. Gent, F. O. Bryan, A. F. Thompson, M. C. Long, and R. Abernathey, 2016: Southern Ocean overturning compensation in an eddy-resolving climate simulation. *J. Phys. Oceanogr.*, 46, 1575–1592, https://doi.org/10.1175/JPO-D-15-0177.1.

Cessi, P., 2019: The global overturning circulation. *Annu. Rev. Mar. Sci.*, **11**, 249–270, https://doi.org/10.1146/annurev-marine-010318-095241.

Ferrari, R., M. F. Jansen, J. F. Adkins, A. Burke, A. L. Stewart, and A. F. Thompson, 2014: Antarctic sea ice control on ocean

- circulation in present and glacial climates. *Proc. Natl. Acad. Sci. USA*, **111**, 8753–8758, https://doi.org/10.1073/pnas.1323922111.
- Gent, P. R., and J. C. McWilliams, 1990: Isopycnal mixing in ocean circulation models. J. Phys. Oceanogr., 20, 150–155, https:// doi.org/10.1175/1520-0485(1990)020<0150:IMIOCM>2.0.CO;2.
- Ito, T., and J. Marshall, 2008: Control of lower-limb overturning circulation in the Southern Ocean by diapycnal mixing and mesoscale eddy transfer. J. Phys. Oceanogr., 38, 2832–2845, https://doi.org/10.1175/2008JPO3878.1.
- Jansen, M. F., and L.-P. Nadeau, 2016: The effect of Southern Ocean surface buoyancy loss on the deep-ocean circulation and stratification. *J. Phys. Oceanogr.*, 46, 3455–3470, https:// doi.org/10.1175/JPO-D-16-0084.1.
- Jones, C. S., and R. P. Abernathey, 2019: Isopycnal mixing controls deep ocean ventilation. *Geophys. Res. Lett.*, 46, 13144–13151, https://doi.org/10.1029/2019GL085208.
- Kamenkovich, I. V., and P. J. Goodman, 2000: The dependence of AABW transport in the Atlantic on vertical diffusivity. Geophys. Res. Lett., 27, 3739–3742, https://doi.org/10.1029/ 2000GL011675.
- Lumpkin, R., and K. Speer, 2007: Global ocean meridional overturning. J. Phys. Oceanogr., 37, 2550–2562, https://doi.org/ 10.1175/JPO3130.1.
- Marshall, J., and K. Speer, 2012: Closure of the meridional overturning circulation through Southern Ocean upwelling. *Nat. Geosci.*, 5, 171–180, https://doi.org/10.1038/ngeo1391.
- —, A. Adcroft, C. Hill, L. Perelman, and C. Heisey, 1997: A finite-volume, incompressible Navier Stokes model for studies of the ocean on parallel computers. *J. Geophys. Res.*, 102, 5753–5766, https://doi.org/10.1029/96JC02775.
- Mashayek, A., R. Ferrari, M. Nikurashin, and W. R. Peltier, 2015: Influence of enhanced abyssal diapycnal mixing on stratification and the ocean overturning circulation. *J. Phys. Oceanogr.*, **45**, 2580–2597, https://doi.org/10.1175/JPO-D-15-0039.1.
- Munk, W. H., 1966: Abyssal recipes. *Deep-Sea Res. Oceanogr. Abstr.*, **13**, 707–730, https://doi.org/10.1016/0011-7471(66)90602-4.
- —, and C. Wunsch, 1998: Abyssal recipes II: Energetics of tidal and wind mixing. *Deep-Sea Res. I*, **45**, 1977–2010, https:// doi.org/10.1016/S0967-0637(98)00070-3.
- Nadeau, L.-P., and M. F. Jansen, 2020: Overturning circulation pathways in a two-basin ocean model. J. Phys. Oceanogr., 50, 2105–2122, https://doi.org/10.1175/JPO-D-20-0034.1.

- Nikurashin, M., and G. Vallis, 2011: A theory of deep stratification and overturning circulation in the ocean. *J. Phys. Oceanogr.*, **41**, 485–502, https://doi.org/10.1175/2010JPO4529.1.
- Shakespeare, C. J., and A. M. Hogg, 2012: An analytical model of the response of the meridional overturning circulation to changes in wind and buoyancy forcing. *J. Phys. Oceanogr.*, **42**, 1270–1287, https://doi.org/10.1175/JPO-D-11-0198.1.
- Shin, S.-I., Z. Liu, B. L. Otto-Bliesner, J. E. Kutzbach, and S. J. Vavrus, 2003: Southern Ocean sea-ice control of the glacial North Atlantic thermohaline circulation. *Geophys. Res. Lett.*, 30, 1096, https://doi.org/10.1029/2002GL015513.
- Stewart, A. L., R. Ferrari, and A. F. Thompson, 2014: On the importance of surface forcing in conceptual models of the deep ocean. *J. Phys. Oceanogr.*, **44**, 891–899, https://doi.org/10.1175/JPO-D-13-0206.1.
- Stommel, H., 1961: Thermohaline convection with two stable regimes of flow. *Tellus*, **13**, 224–230, https://doi.org/10.3402/tellusa.v13i2.9491.
- ——, and A. B. Arons, 1959: On the abyssal circulation of the world ocean: I. Stationary planetary flow patterns on a sphere. *Deep-Sea Res.*, **6**, 140–154, https://doi.org/10.1016/0146-6313(59) 90065-6.
- Sun, S., I. Eisenman, and A. L. Stewart, 2016: The influence of Southern Ocean surface buoyancy forcing on glacialinterglacial changes in the global deep ocean stratification. *Geophys. Res. Lett.*, 43, 8124–8132, https://doi.org/ 10.1002/2016GL070058.
- Talley, L. D., 2013: Closure of the global overturning circulation through the Indian, Pacific, and Southern Oceans: Schematics and transports. *Oceanography*, 26, 80–97, https://doi.org/10.5670/ oceanog.2013.07.
- Toggweiler, J., and B. Samuels, 1995: Effect of Drake Passage on the global thermohaline circulation. *Deep-Sea Res. I*, **42**, 477–500, https://doi.org/10.1016/0967-0637(95)00012-U.
- Watson, A. J., G. K. Vallis, and M. Nikurashin, 2015: Southern Ocean buoyancy forcing of ocean ventilation and glacial atmospheric CO₂. *Nat. Geosci.*, 8, 861–864, https://doi.org/ 10.1038/ngeo2538.
- Young, W. R., 2012: An exact thickness-weighted average formulation of the Boussinesq equations. *J. Phys. Oceanogr.*, **42**, 692–707, https://doi.org/10.1175/JPO-D-11-0102.1.